J|A|C|S
ARTICLES
Published on Web 03/11/2006

Probing the Intrinsic Electronic Structure of the Bis(dithiolene) Anions $[M(mnt)_2]^{2-}$ and $[M(mnt)_2]^{1-}$ (M = Ni, Pd, Pt; mnt = 1,2-$S_2C_2(CN)_2$) in the Gas Phase by Photoelectron Spectroscopy

Tom Waters, Hin-Koon Woo, Xue-Bin Wang, and Lai-Sheng Wang*

Contribution from the Department of Physics, Washington State University, 2710 University Drive, Richland, Washington 99354, and W. R. Wiley Environmental Molecular Sciences Laboratory and Chemical Sciences Division, Pacific Northwest National Laboratory, P.O. Box 999, Richland, Washington 99352

Received September 14, 2005; E-mail: ls.wang@pnl.gov

Abstract: A detailed understanding of the electronic structure of transition metal bis(dithiolene) complexes is important because of their interesting redox, magnetic, optical, and conducting properties and their relevance to enzymes containing molybdenum and tungsten bis(dithiolene) centers. The electronic structures of the bis(dithiolene) anions $[M(mnt)_2]^{n-}$ (M = Ni, Pd, Pt; mnt = 1,2-$S_2C_2(CN)_2$; $n = 0-2$) were examined by a combination of photodetachment photoelectron spectroscopy (PES) and density functional theory calculations. The combined experimental and theoretical data provide insight into the molecular orbital energy levels of $[M(mnt)_2]^{2-}$ and the ground and excited states of $[M(mnt)_2]^{1-}$ and $[M(mnt)_2]$. Detachment features from ligand-based orbitals of $[M(mnt)_2]^{2-}$ occur at similar energies for each species, independent of the metal center, while those arising from metal-based orbitals occur at higher energies for the heavier congeners. Electronic excitation energies inferred for $[M(mnt)_2]^{1-}$ from the PES experiments agree well with those obtained in optical absorption experiments in solution, with the PES experiments providing additional insight into the changes in energy of these transitions as a function of metal. The singly charged anions $[M(mnt)_2]^{1-}$ were also prepared and studied independently. Electron detachment from the ground states of these doublet anions accessed the lowest singlet and triplet states of neutral $[M(mnt)_2]$, thereby providing a direct experimental measure of their singlet−triplet splitting.

Introduction

Nickel bis(dithiolene) complexes $[Ni(S_2C_2R_2)_2]^{n-}$ have attracted considerable attention as a result of their interesting redox, magnetic, optical, and conducting properties,[1−6] unique reactivity,[1,7,8] and relevance to important bioinorganic centers.[1,9] Many of the properties of these systems stem from their unusual and complex electronic structures, which have been the focus of sustained experimental and theoretical interest.[10] Early studies identified the existence of the reversible three-member one-electron transfer series $[Ni(S_2C_2R_2)_2]^{2-} \leftrightarrow [Ni(S_2C_2R_2)_2]^{1-} \leftrightarrow [Ni(S_2C_2R_2)_2]$, in which each member maintains a square planar geometry.[11−14] The redox chemistry of this series is complicated by a subtle interplay between ligand- and metal-based redox chemistry ("noninnocence"[15]) and a significant degree of mixing between metal and ligand based orbitals (metal-sulfur covalency). The redox active orbital is an out-of-plane orbital that is predominantly ligand based (S $3p_z$) but with some metal character (Ni $3d_{xz}$; Figure 1, b_{2g}). The nature of this orbital has been probed in detail by EPR[16,17] and ENDOR/ESEEM spectroscopies[18] and, more recently, sulfur K-edge X-ray absorption spectroscopy.[19] These studies indicate ~60% S 3p character in this orbital and demonstrate the noninnocent nature of the dithiolene ligand.

(1) *Dithiolene Chemistry: Synthesis, Properties and Applications* (Steifel, E. I.; Ed.) In *Progress in Inorganic Chemistry* (Karlin, K. D.; Series Ed.) Vol. 52, Wiley: New York, 2003, 738 pages.
(2) Robertson, N.; Cronin, L. *Coord. Chem. Rev.* **2002**, *227*, 93.
(3) Fourmigue, M. *Acc. Chem. Res.* **2004**, *37*, 179.
(4) Kato, R. *Chem. Rev.* **2004**, *104*, 5319.
(5) Cassoux, P. *Coord. Chem. Rev.* **1999**, *186*, 213.
(6) Faulmann, C.; Cassoux, P. *Solid-State Properties (Electronic, Magnetic, Optical) of Dithiolene Complex-Based Compounds* In ref 1; p 399.
(7) Wing, R. M.; Tustin, G. C.; Okamura, W. H. *J. Am. Chem. Soc.* **1970**, *92*, 1935.
(8) Wang, K.; Stiefel, E. I. *Science* **2001**, *291*, 106.
(9) Enemark, J. H.; Cooney, J. J. A.; Wang, J. J.; Holm, R. H. *Chem. Rev.* **2004**, *104*, 1175.
(10) Kirk, M. L.; McNaughton, R. L.; Helton, M. E. *The Electronic Structure and Spectroscopy of Metallo-Dithiolene Complexes* In ref 1; pp 111.
(11) Davison, A.; Edelstein, N.; Holm, R. H.; Maki, A. H. *J. Am. Chem. Soc.* **1963**, *85*, 2029.
(12) Davison, A.; Edelstein, N.; Holm, R. H.; Maki, A. H. *Inorg. Chem.* **1963**, *2*, 1227.
(13) McCleverty, J. A., *Prog. Inorg. Chem.* **1968**, *10*, 49.
(14) Schrauzer, G. N. *Acc. Chem. Res.* **1969**, *2*, 72.
(15) Ward, M. D.; McCleverty, J. A. *J. Chem. Soc., Dalton Trans.* **2002**, 275.
(16) Maki, A. H.; Edelstein, N.; Davison, A.; Holm, R. H. *J. Am. Chem. Soc.* **1964**, *86*, 4580.
(17) Schmitt, R. D.; Maki, A. H. *J. Am. Chem. Soc.* **1968**, *90*, 2288.
(18) Huyett, J. E.; Choudhury, S. B.; Eichhorn, D. M.; Bryngelson, P. A.; Maroney, M. J.; Hoffman, B. M. *Inorg. Chem.* **1998**, *37*, 1361.
(19) Szilagyi, R. K.; Lim, B. S.; Glaser, T.; Holm, R. H.; Hedman, B.; Hodgson, K. O.; Solomon, E. I. *J. Am. Chem. Soc.* **2003**, *125*, 9158.

 10.1021/ja056342s CCC: $33.50

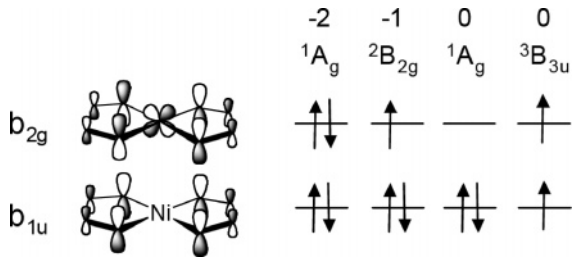

Figure 1. Frontier orbitals of $[Ni(S_2C_2R_2)]^{n-}$ centers ($n = 2, 1, 0$) relevant to their redox and low-energy electronic absorption properties. The ground-state electronic configurations of the dianion, anion, and neutral are shown, as well as the lowest-energy triplet state of the neutral.

A common feature of the $[Ni(S_2C_2R_2)_2]^{2-/1-/0}$ series is the observation of an intense low-energy absorption for the anionic and neutral species that is not observed for the reduced dianionic member. This is assigned to a dipole allowed transition from a ligand based out-of-plane orbital (Figure 1, b_{1u}) to the redox active orbital that is singly occupied and vacant in the anion and neutral forms, respectively, but doubly occupied in the dianionic form (Figure 1).[10] The energy and intensity of this absorption are relevant to the optical applications of dithiolenes, e.g., as near-IR dyes for Q-switched lasers, and many studies have aimed to tune this absorption by variation of the metal or ligand.[20−23]

Two alternative bonding descriptions have been proposed for the neutral form $[Ni(S_2C_2R_2)]$ and involve either (i) two ligand radicals whose spins are antiferromagnetically coupled (singlet diradical) or (ii) a delocalized resonance pair with one neutral dithioketene and one dianionic dithiolene ligand.[13,14,24−26] Both descriptions are compatible with the experimentally observed singlet ground state. The energetic separation between the singlet and triplet states (Figure 1, ^1A_g and $^3B_{3u}$, respectively) has been proposed as an indication of the extent of singlet-diradical character in the ground-state wave function[27−29] and has been estimated to be in the range 0.5−1.2 eV using a variety of theoretical techniques.[19,27−29] Experimental data do not appear to be available but are important in order to evaluate the different bonding descriptions as well as the different theoretical approaches that have been applied to these systems.

Photodetachment photoelectron spectroscopy (PES) allows the electronic structure of gaseous anionic species to be investigated, providing detailed information about molecular orbital (MO) energy levels of the parent species and the ground and excited states of the ionized species. The coupling of an electrospray source to a photoelectron spectrometer[30] has allowed a number of negatively charged solution phase species to be studied for the first time in the gas phase,[31,32] including a number of oxomolybdenum-bis(dithiolene) centers.[33,34] The present study describes the use of electrospray to transfer the anions $[M(mnt)_2]^{2-}$ and $[M(mnt)_2]^{1-}$ (M = Ni, Pd, Pt; mnt = $S_2C_2(CN)_2$) from solution to the gas phase, where their electronic structures were studied by PES. The electron withdrawing cyanide substituents on the dithiolene ligand were chosen to ensure that the dianions were stable gas-phase species (i.e., stable with respect to electron detachment).[34] Experimental data were interpreted with the aid of density functional theory (DFT) calculations on the ground states of $[M(mnt)_2]^{2-,1-,0}$ and the ground and excited states of $[M(mnt)_2]$.$^{1-,0}$ The combined data provide direct insights into the electronic structure of each member of the electron-transfer series $[M(mnt)_2]^{2-/1-/0}$ (M = Ni, Pd, Pt).

Experimental and Theoretical Details

Photodetachment Photoelectron Spectroscopy. The PES experiments were carried out on two home-built instruments that couple an electrospray source to a magnetic bottle time-of-flight photoelectron spectrometer. The anions $[M(mnt)_2]^{2-}$ and $[M(mnt)_2]^{1-}$ (M = Ni, Pd or Pt) were generated by electrospray from solutions of $(Bu_4N)_2[M(mnt)_2]$ in solvent CH_3CN ($\sim$0.1 mg mL^{-1}).[35] The singly charged anions $[M(mnt)_2]^{1-}$ were formed by one-electron oxidation of $[M(mnt)_2]^{2-}$ during the electrospray process.

Experiments on the monoanions $[M(mnt)_2]^{1-}$ were carried out on an electrospray PES instrument that has been described in detail elsewhere.[30] Experiments on the dianions $[M(mnt)_2]^{2-}$ were carried out on a newly developed instrument that allows for higher resolution spectra due to the ability to cool ions to low temperatures to remove vibrational hot bands.[36,37] The higher resolution was necessary for the dianions due to the high kinetic energies of the detached electrons as a result of their low electron binding energies and the presence of the repulsive coulomb barrier (RCB) for electron detachment from these multiply charged species.[38−42] Anions from the source were guided by an RF-only octopole device into a quadrupole mass filter (operated in the RF-only mode in the current experiment) and then guided by a 90° ion bender into the cooled 3D ion trap. The trap is attached to the cold head of a cryostat, which consists of a closed-cycle helium refrigerator and a feedback heating system, and allows temperatures to be controlled from 10 to 400 K. The trap was operated at 70 K in the current experiments. The incoming ions were trapped and collisionally cooled by $\sim$1 mTorr N_2 background gas for a period of 20−100 ms ($\sim$(2−10) $\times$ 10^3 collisions). Previous experiments

(20) Mueller-Westerhoff, U.; Vance, B.; Yoon, D. I. *Tetrahedron* **1991**, *47*, 909.
(21) Deplano, P.; Mercuri, M. L.; Pintus, G.; Trogu, E. F. *Comments Inorg. Chem.* **2001**, *22*, 353.
(22) Aragoni, M. C.; Arca, M.; Demartin, F.; Devillanova, F. A.; Garau, A.; Isaia, F.; Lelj, F.; Lippolis, V.; Verani, G. *J. Am. Chem. Soc.* **1999**, *121*, 7098.
(23) Aragoni, M. C.; Arca, M.; Cassano, T.; Denotti, C.; Devillanova, F. A.; Frau, R.; Isaia, F.; Lelj, F.; Lippolis, V.; Nitti, L.; Romaniello, P.; Tommasi, R.; Verani, G. *Eur. J. Inorg. Chem.* **2003**, 1939.
(24) Stiefel, E. I.; Waters, J. H.; Billig, E.; Gray, H. B. *J. Am. Chem. Soc.* **1965**, *87*, 3016.
(25) Balch, A. L.; Holm, R. H. *J. Am. Chem. Soc.* **1966**, *88*, 5201.
(26) Holm, R. H.; Olanov, M. J. *Prog. Inorg. Chem.* **1971**, *14*, 241.
(27) Lauterbach, C.; Fabian, J. *Eur. J. Inorg. Chem.* **1999**, 1995.
(28) Bachler, V.; Olbrich, G.; Neese, F.; Wieghardt, K. *Inorg. Chem.* **2002**, *41*, 4179.
(29) Ray, K.; Weyhermuller, T.; Neese, F.; Wieghardt, K. *Inorg. Chem.* **2005**, *44*, 5345.
(30) Wang, L. S.; Ding, C. F.; Wang, X. B.; Barlow, S. E. *Rev. Sci. Instrum.* **1999**, *70*, 1957.
(31) Wang, L. S.; Wang, X. B. *J. Phys. Chem. A* **2000**, *104*, 1978.
(32) Wang, X. B.; Yang, X.; Wang, L. S. *Int. Rev. Phys. Chem.* **2002**, *21*, 473.
(33) Wang, X. B.; Inscore, F. E.; Yang, X.; Cooney, J. J. A.; Enemark, J. H.; Wang, L. S. *J. Am. Chem. Soc.* **2002**, *124*, 10182.
(34) Waters, T.; Wang, X. B.; Yang, X.; Zhang, L.; O'Hair, R. A. J.; Wang, L. S.; Wedd, A. G. *J. Am. Chem. Soc.* **2004**, *126*, 5119.
(35) Billig, E.; Williams, R.; Bernal, I.; Waters, J. H.; Gray, H. B. *Inorg. Chem.* **1964**, *3*, 663.
(36) Wang, X. B.; Woo, H. K.; Kiran, B.; Wang, L. S. *Angew. Chem., Int. Ed.* **2005**, *44*, 4968.
(37) Wang, X. B.; Woo, H. K.; Wang, L. S. *J. Chem. Phys.* **2005**, *123*, 051106.
(38) Wang, X. B.; Ding, C. F.; Wang, L. S. *Phys. Rev. Lett.* **1998**, *81*, 3351.
(39) Wang, L. S.; Ding, C. F.; Wang, X. B.; Nicholas, J. B. *Phys. Rev. Lett.* **1998**, *81*, 2667.
(40) Wang, X. B.; Wang, L. S. *J. Am. Chem. Soc.* **2000**, *122*, 2339.
(41) Wang, L. S.; Wang, X. B. *J. Phys. Chem. A* **2000**, *104*, 1978.
(42) Dreuw, A.; Cederbaum, L. S. *Chem. Rev.* **2002**, *102*, 181.

suggest that under these conditions an effective ion temperature of 70−100 K can be achieved.[36,37] The ions were pulsed out of the trap into the extraction zone of a time-of-flight mass spectrometer at a 10 Hz repetition rate. Ions of interest were mass selected and decelerated before being intercepted by a detachment laser beam (193 nm from an ArF excimer laser or 266 and 355 nm from a Nd:YAG laser) in the interaction zone of a magnetic-bottle photoelectron analyzer. The lasers were operated at a 20 Hz repetition rate with the ion beam off at alternate shots for background subtraction. Photoelectrons were collected with high efficiency by the magnetic-bottle and analyzed in a 5.2-m long electron flight tube. Photoelectron time-of-flight spectra were collected and then converted into kinetic energy spectra, calibrated by the known spectra of I^- and ClO_2^-.[43] Electron binding energy spectra were obtained by subtracting the kinetic energy spectra from the detachment photon energies. The energy resolution ($\Delta E/E$) was estimated as approximately 2% (fwhm), i.e., approximately 20 meV for 1 eV electrons, as measured from the spectra of I^- at 355 nm. Due to the lack of vibrational resolution, adiabatic detachment energies (ADEs) were measured from the leading edge of the threshold band and then adding a constant to take into account for instrumental resolution. The removal of vibrational hot bands due to the vibrational cooling resulted in sharp spectral onsets and allowed for reasonably accurate and consistent ADEs to be obtained. Vertical detachment energies (VDEs) were measured from the peak maxiumum.

Theoretical Calculations. Density functional theory (DFT) calculations were carried out at the BP86 level of theory,[44,45] which has been shown to give reasonable description of the geometric and electronic structure of a similar series of nickel bis(dithiolene) complexes $[Ni(S_2C_2Me_2)_2]^{n-}$ ($n = 0-2$).[19,46] In particular, this functional was shown to give a reasonable description of the sulfur 3p character in the frontier orbitals of $[Ni(S_2C_2Me_2)_2]^{n-}$ by comparison with experimental sulfur K-edge X-ray absorption data.[19] Calculations employed the 6-311+G* basis sets for C, N, and S and the Stuttgart quasi-relativistic effective core potentials and basis sets augmented with two f-type and one g-type polarization functions for Ni, Pd, and Pt.[47,48] Calculations were carried out using the NWChem 4.6 program at the Molecular Science Computing Facility located at the W. R. Wiley Environmental Molecular Sciences Laboratory.[49] Three-dimensional contours of the calculated molecular orbitals were generated using the Extensible Computational Chemistry Environment (Ecce) software.[50]

Geometries of $[M(mnt)_2]^{2-}$ and $[M(mnt)_2]^{1-}$ were optimized under constrained D_{2h} point symmetry as is observed in the solid state.[51] Cartesian axes were chosen such that the molecule lies in the *xy* plane with the *x*-axis bisecting the C−C bond of the dithiolene chelate rings. Cartesian coordinates for the optimized geometries are included in the Supporting Information (Tables S1, S2). The first VDEs for $[M(mnt)_2]^{2-}$ and $[M(mnt)_2]^{1-}$ were calculated by the ΔSCF method, i.e., the difference in energy between the ground states of the parent and one-electron detached species with its geometry fixed at that of the parent. VDEs for higher binding energy detachment features were calculated from the difference in energy between the parent species and excited states of the one-electron detached species, calculated using time-dependent density functional theory (TD-DFT).[52−54] The photoelectron spectra are interpreted within the framework of one-electron detachment transitions, with spectral features assumed to arise from direct electron detachment from occupied orbitals of the parent species. Consequently, only excited states involving electronic transitions to molecular orbitals that are occupied in the parent species should be accessible, and those arising from transitions to orbitals that are vacant in the parent species are not expected to be observed or should be extremely weak.

Experimental Results

Photoelectron Spectra of $[M(mnt)_2]^{2-}$ (M = Ni, Pd, Pt). PES spectra, recorded at three different photon energies for each of $[M(mnt)_2]^{2-}$, are presented in Figures 2−4. The first detachment feature is labeled X, and the remaining detachment features are labeled A, B, etc. in order of increasing energy. Adiabatic and vertical detachment energies are detailed in Table 1.

The lower photon energy spectra show fewer features, but with better resolution due to the lower kinetic energies of the photoelectrons. The spectra recorded at 266 and 355 nm were complicated by the fact that $[M(mnt)_2]^{2-}$ anions are strongly absorbing at these photon energies,[55,56] giving rise to the possibility of autodetachment transitions and the appearance of non-Franck−Condon detachment features (Figures 2, 4; labeled *). These are presumed to arise through absorption of a photon by $[M(mnt)_2]^{2-}$ to a metastable electronically excited state of the parent dianion that lies above the detachment threshold, which can undergo significant vibrational relaxation prior to electron detachment. Such autodetachment features are especially severe in the 266 and 355 nm spectra of $[Ni(mnt)_2]^{2-}$ and $[Pt(mnt)_2]^{2-}$, as can be seen from the broad signals between the features labeled X and A in each spectrum (Figures 2, 4). Strong autodetachment features were previously observed in the 266 nm spectra of C_{60}^- and Au_{20}^-.[57,58]

A. Repulsive Coulomb Barrier. The spectra for $[M(mnt)_2]^{2-}$ are truncated at binding energies about 1.5−2.0 eV below the photon energy in each case (Figures 2−4) due to the repulsive Coulomb barrier (RCB), a general feature of photodetachment from multiply charged anions.[38−42] This arises from the superposition of short range electron attachment and long range coulomb repulsion between the two negatively charged photoproducts (e.g., $A^{2-} \rightarrow A^- + e^-$) and results in the disappearance of high binding energy features in the lower photon energy spectra due to outgoing electrons having insufficient kinetic energies to surmount this barrier.[38−42] For example, features D, E, and F for

(43) Gilles, M. K.; Polak, M. L.; Lineberger, W. C. *J. Chem. Phys.* **1992**, *96*, 8012.
(44) Perdew, J. P. *Phys. Rev. B* **1986**, *33*, 8822.
(45) Becke, A. D. *Phys. Rev. A* **1988**, *38*, 3098.
(46) Lim, B. S.; Fomitchev, D. V.; Holm, R. H. *Inorg. Chem.* **2001**, *40*, 4257.
(47) (a) Dolg, M.; Wedig, U.; Stoll, H.; Preuss, H. *J. Chem. Phys.* **1987**, *86*, 866. (b) Andrae, D.; Haeussermann, Y.; Dolg, M.; Stoll, H.; Preuss, H. *Theor. Chim. Acta* **1990**, *77*, 123.
(48) Martin, J. M. L.; Sundermann, A. *J. Chem. Phys.* **2001**, *114*, 3408.
(49) (a) Aprà, E. et al. *NWChem, A Computational Chemistry Package for Parallel Computers*, version 4.6; Pacific Northwest National Laboratory, Richland, WA 99352-0999, USA, 2004. (b) Kendall, R. A. et al. High Performance Computational Chemistry: an Overview of NWChem a Distributed Parallel Application. *Computer Phys. Comm.* **2000**, *128*, 260.
(50) Black, G. et al. *Ecce, A Problem Solving Environment for Computational Chemistry*, Software Version 3.2.2; Pacific Northwest National Laboratory, Richland, WA, 99352-0999, USA.
(51) Beswick, C. L.; Schulman, J. M.; Stiefel, E. I. *Structures and Structural Trends in Homoleptic Dithiolene Complexes*; in ref 1; p 55.
(52) Bauernschmitt, R.; Ahlrichs, R. *Chem. Phys. Lett.* **1996**, *256*, 454.
(53) Jamorski, C.; Casida, M. E.; Salahub, D. R. *J. Chem. Phys.* **1996**, *104*, 5134.
(54) Bauernschmitt, R.; Haser, M.; Treutler, O.; Ahlrichs, R. *Chem. Phys. Lett.* **1997**, *264*, 573.
(55) Shupack, S. I.; Billig, E.; Clark, R. J. H.; Williams, R.; Gray, H. B. *J. Am. Chem. Soc.* **1964**, *86*, 4594.
(56) Chandramouli, G. V. R.; Manoharan, P. T. *Inorg. Chem.* **1986**, *25*, 4680.
(57) Wang, X. B.; Ding, C. F.; Wang, L. S. *J. Chem. Phys.* **1999**, *110*, 8217.
(58) Li, J.; Li, X.; Zhai, H. J.; Wang, L. S. *Science* **2003**, *299*, 864.

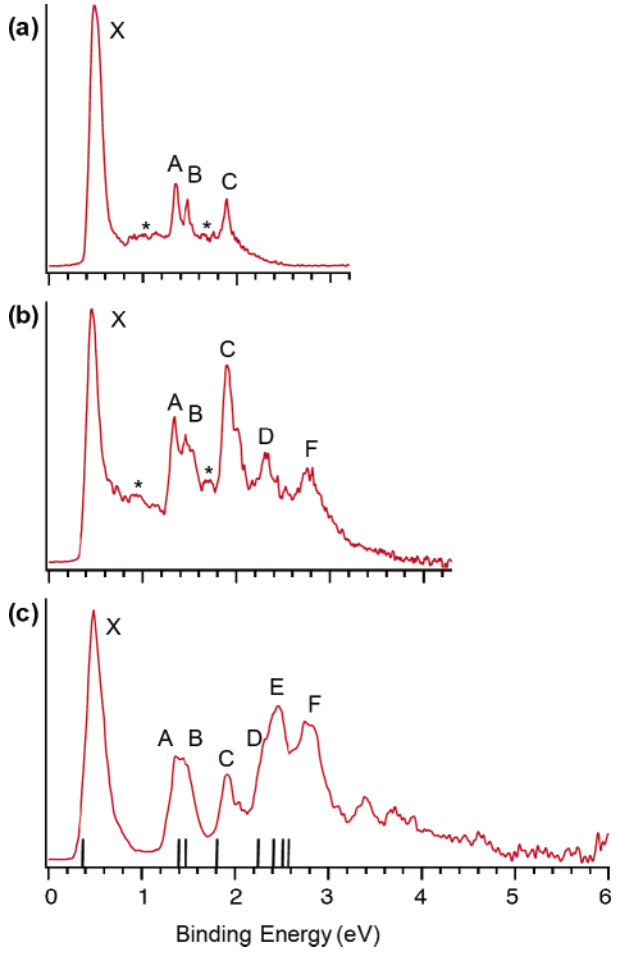

Figure 2. Photoelectron spectra of $[Ni(mnt)_2]^{2-}$ at (a) 355, (b) 266, and (c) 193 nm. The vertical bars in (c) represent the theoretically predicted positions of vertical detachment transitions from the HOMO to HOMO-7 levels (Table 4). Features marked with an asterisk in the 266 and 355 nm spectra are not observed at 193 nm and are assumed to be due to autodetachment or multielectron processes.

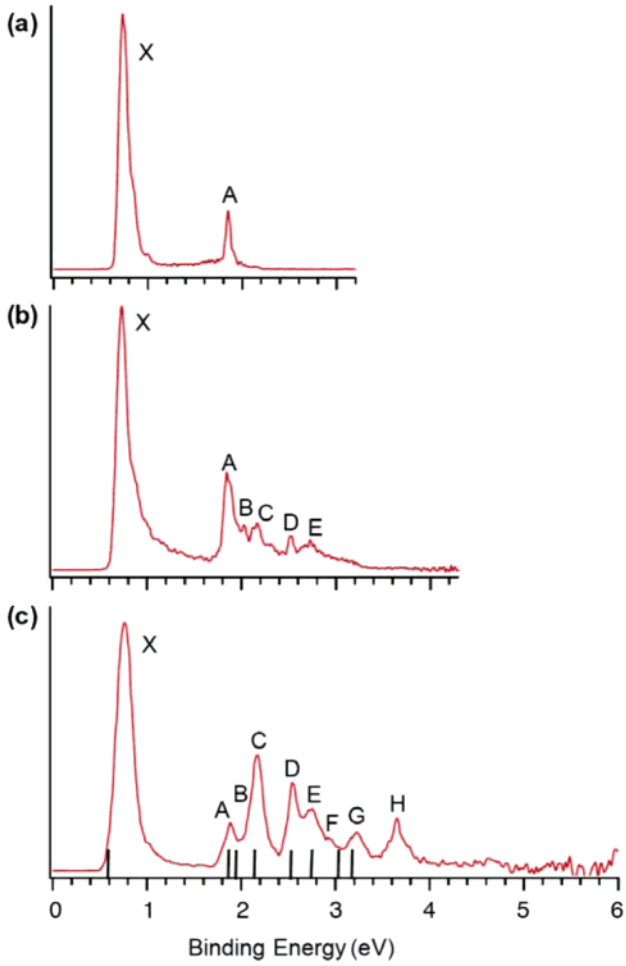

Figure 3. Photoelectron spectra of $[Pd(mnt)_2]^{2-}$ at (a) 355, (b) 266, and (c) 193 nm. The vertical bars in (c) represent the theoretically predicted positions of vertical detachment transitions from the HOMO to HOMO-7 levels (Table 4).

$[Ni(mnt)_2]^{2-}$ were observed in the 193 nm spectrum in the range 2.3−2.8 eV (Figure 2) but were not observed in the 355 nm spectrum despite the photon energy (3.496 eV) exceeding the binding energies of these features.

B. $[Ni(mnt)_2]^{2-}$. Feature X occurs at a VDE of 0.49 eV (Figure 2). The features labeled A and B are more clearly resolved into two separate features in the 266 and 355 nm spectra. A small peak occurring between features B and C in the 266 nm spectrum does not appear in the 193 nm spectrum and is likely due to an autodetachment or multielectron transition. Feature C is significantly more intense in the 266 nm spectrum than at 193 or 355 nm. The two features labeled E and F in the 193 nm spectrum are broader and may arise from the superposition of multiple detachment transitions. The intensity of feature E is significantly reduced at 266 nm, revealing a weaker shoulder labeled D on its low binding energy side. These features are absent in the 355 nm spectrum due to the RCB, as described above.

C. $[Pd(mnt)_2]^{2-}$. Feature X occurs at a VDE of 0.73 eV, about 0.24 eV higher than that for $[Ni(mnt)_2]^{2-}$ (Table 1). Three features labeled A, B, and C all occur at similar binding energies in the region 1.8−2.2 eV (Figure 3). The relative intensity of feature A is much higher at 266 nm compared with that at 193 nm. Feature B is not evident at 193 nm but appears as a weak feature at 266 nm (Figure 3b). Features D and E are both much weaker at 266 nm.

D. $[Pt(mnt)_2]^{2-}$. Feature X occurs at a VDE of 0.51 eV, about 0.22 eV lower than that for $[Pd(mnt)_2]^{2-}$ and almost identical to that for $[Ni(mnt)_2]^{2-}$ (Table 1). Feature A in the 193 nm spectrum exhibits two shoulders on the high binding energy side (B, C), which are more clearly resolved at 266 nm (Figure 4). The relative intensity of feature B is significantly higher at 266 nm. A broad feature centered around 2.3 eV is evident in the 355 nm spectrum but is not present at 193 or 266 nm and is assumed to be due to autodetachment. Feature D at a VDE of 2.50 eV is the sharpest and most intense feature at 193 nm but becomes significantly weaker at 266 nm. Two well-defined and broad features labeled E and F are observed in the 193 nm spectrum but are not observed at 266 nm and are likely cut off due to the RCB. The broad features on the higher binding energy side of feature D at 266 nm are likely due to autodetachment.

Photoelectron Spectra of $[M(mnt)_2]^{1-}$ (M = Ni, Pd, Pt). Photoelectron spectra of the singly charged anions $[M(mnt)_2]^{1-}$ at 193 nm are presented in Figure 5. These monoanionic complexes possess significantly higher electron binding energies than those for the dianions due to the absence of coulomb repulsion and consequently could only be studied at 193 nm. The spectra for these singly charged anions appear quite congested beyond the first feature (X) and might be comprised of numerous overlapping features. The major features are labeled X and A−C, and their VDEs are summarized in Table 2.

The change in energy of the first detachment feature with variation of the metal in $[M(mnt)_2]^{1-}$ is less pronounced than that observed for the dianions $[M(mnt)_2]^{2-}$. This first feature occurs at nearly identical binding energies for $[Ni(mnt)_2]^{1-}$ and $[Pd(mnt)_2]^{1-}$ and ∼0.1 eV lower for $[Pt(mnt)_2]^{1-}$ (Table 2). The separation between features X and A is 0.79, 0.57, and 0.83 eV for M = Ni, Pd, and Pt, respectively (Table 2).

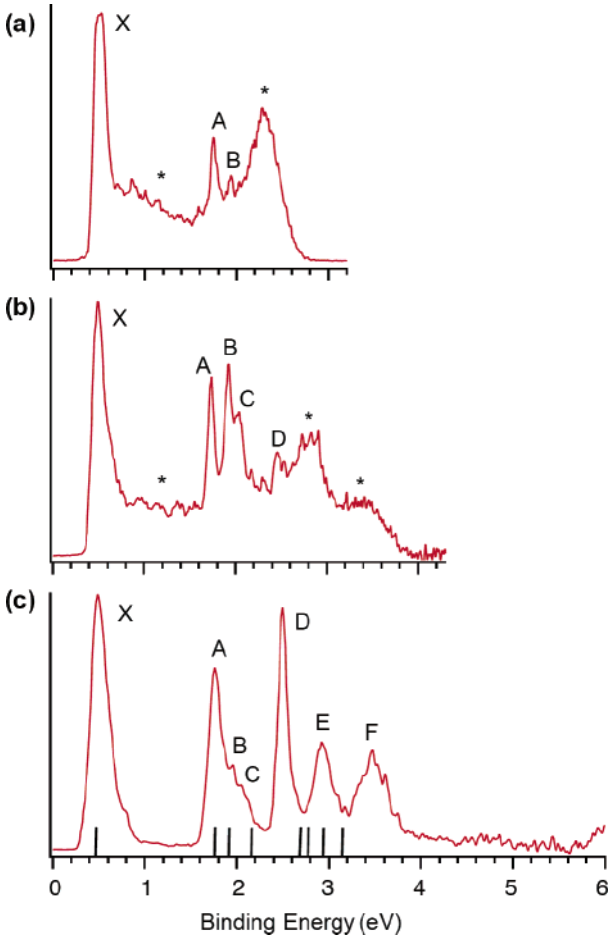

Figure 4. Photoelectron spectra of $[Pt(mnt)_2]^{2-}$ at (a) 355, (b) 266, and (c) 193 nm. The vertical bars in (c) represent the theoretically predicted positions of vertical detachment transitions from the HOMO to HOMO-7 levels (Table 4). Features marked with an asterisk in the 266 and 355 nm spectra are not observed at 193 nm and are assumed to be due to autodetachment or multielectron processes.

Table 1. Experimental Adiabatic (ADE) and Vertical (VDE) Detachment Energies (eV) for the Dianions $[M(mnt)_2]^{2-}$ (M = Ni, Pd, Pt)[a]

	feature	$[Ni(mnt)_2]^{2-}$	$[Pd(mnt)_2]^{2-}$	$[Pt(mnt)_2]^{2-}$
ADE		0.44(4)	0.69(4)	0.46(4)
VDE	X	0.49(3)	0.73(3)	0.51(3)
	A	1.35(3)	1.87(3)	1.75(3)
	B	1.48(3)	2.03(5)	1.94(3)
	C	1.90(3)	2.16(3)	2.05(4)
	D	2.30(5)	2.53(4)	2.50(3)
	E	2.45(10)	2.73(4)	2.92(3)
	F	2.80(10)	2.95(5)	3.48(4)
	G		3.23(4)	
	H		3.66(4)	

[a] The numbers in parentheses represent the uncertainty in the last digit.

Theoretical Results

The geometries of $[M(mnt)_2]^{2-}$ and $[M(mnt)_2]^{1-}$ were optimized under constrained D_{2h} point symmetry, as is observed in the solid state.[51,59,60] Cartesian coordinates are included in the Supporting Information (Tables S1, S2). The calculated structural parameters agree well with those determined experimentally by X-ray crystallography.[51,59,60] M−S bond lengths

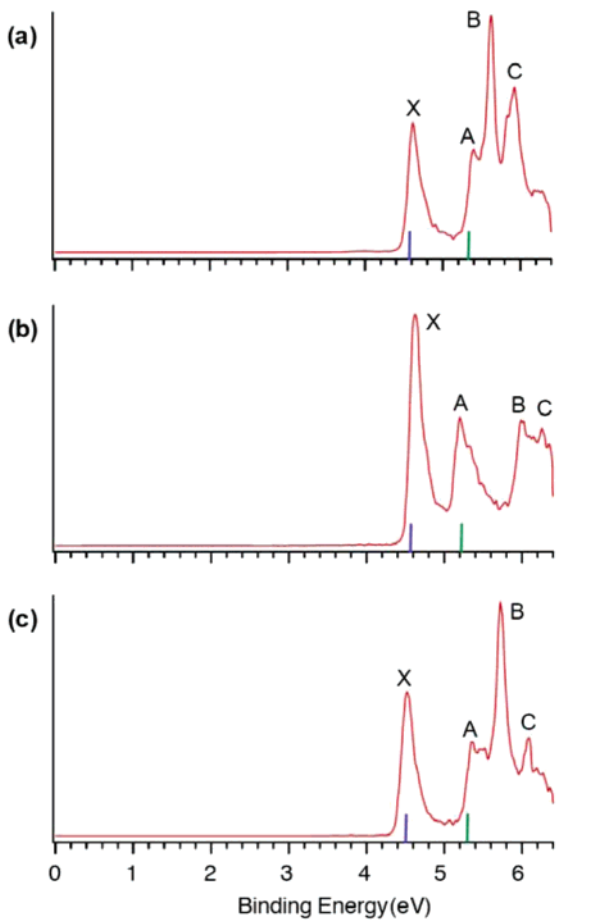

Figure 5. Photoelectron spectra at 193 nm of (a) $[Ni(mnt)_2]^{1-}$, (b) $[Pd(mnt)_2]^{1-}$, and (c) $[Pt(mnt)_2]^{1-}$. The vertical bars represent the calculated VDEs to the lowest energy singlet (blue) and triplet (green) states of the product $[M(mnt)_2]$ (Table 5).

Table 2. Experimental Adiabatic (ADE) and Vertical (VDE) Detachment Energies (eV) for the Anions $[M(mnt)_2]^{1-}$ (M = Ni, Pd, Pt)[a]

	feature	$[Ni(mnt)_2]^{1-}$	$[Pd(mnt)_2]^{1-}$	$[Pt(mnt)_2]^{1-}$
ADE		4.56(4)	4.55(4)	4.45(4)
VDE	X	4.61(3)	4.63(3)	4.52(3)
	A	5.40(4)	5.20(4)	5.35(4)
	B	5.63(4)	6.00(5)	5.72(4)
	C	5.92(5)	6.25(5)	6.09(4)

[a] The numbers in parentheses represent the uncertainty in the last digit.

are slightly longer than those observed in the solid state, as has been observed in DFT calculations on related species.[29,46] M−S bond lengths for $[Ni(mnt)_2]^{2-}$ (2.21 Å) are shorter than those for $[Pd(mnt)_2]^{2-}$ and $[Pt(mnt)_2]^{2-}$ (both 2.34 Å), which are similar due to relativistic bond contraction in the latter.[27] M−S bond lengths were predicted to shorten with oxidation (e.g., Ni−S: 2.21 to 2.18 Å), consistent with the nature of the redox active orbital (b_{2g}, Figure 1), available solid-state structures,[51,59,60] and experimental and theoretical data for closely related systems.[19,29,46]

The eight highest energy occupied orbitals of $[Ni(mnt)_2]^{2-}$ are illustrated in Figure 6 (HOMO−HOMO-7). These orbitals are qualitatively very similar to those calculated previously for $[Ni(S_2C_2Me_2)_2]^{2-}$,[19,46] and detailed discussions of their origin, symmetry, and composition can be found in that work[19,46] and elsewhere.[10,29] Briefly, orbitals comprised of sulfur $3p_z$ atomic

(59) Clemenson, P. I. *Coord. Chem. Rev.* **1990**, *106*, 171.
(60) Kobayashi, A.; Sasaki, Y. *Bull. Chem. Soc. Jpn.* **1977**, *50*, 2650.

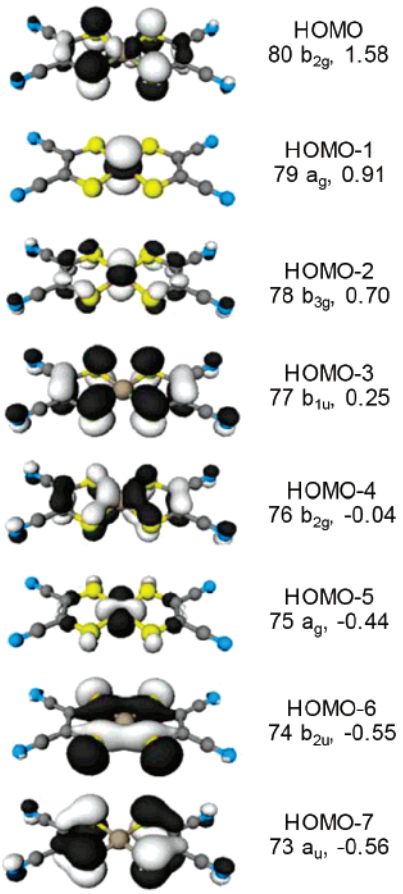

Figure 6. Molecular orbital contour plots (contour cutoff = 0.03) for the eight highest occupied orbitals of $[Ni(mnt)_2]^{2-}$. Orbital symmetries and energies (eV) are included.

orbitals that are orthogonal to the Ni—S bond vector also feature varying contributions from C 2p atomic orbitals involved in the C═C bond (π or π^*). Some of these are also of the correct symmetry to interact with Ni $3d_{xz}$ and $3d_{yz}$ orbitals (e.g., HOMO 80 b_{2g}), while others contain no metal contribution (e.g., HOMO-3 77 b_{1u}). The HOMO-6 is derived from S 3p orbitals directed along the Ni—S bond vector. The HOMO-1 and HOMO-5 are both metal-based and nonbonding (d_{z^2} and $d_{x^2-y^2}$, respectively).

Calculations indicated that the equivalent orbitals of $[Pd(mnt)_2]^{2-}$ and $[Pt(mnt)_2]^{2-}$ were qualitatively similar to those of $[Ni(mnt)_2]^{2-}$, and MO pictures are included in the Supporting Information (Figures S1, S2). A correlation diagram relating the energies of these orbitals with variation of the metal center is provided in Figure 7. This reveals significant changes in the energies of some orbitals (e.g., HOMO-1 and HOMO-2 of $[Ni(mnt)_2]^{2-}$) and little change for others (e.g., HOMO-3).

Vertical electron detachment from the HOMO of singlet $[M(mnt)_2]^{2-}$ accesses the doublet ground state of $[M(mnt)_2]^{1-}$ with its geometry fixed at that of $[M(mnt)_2]^{2-}$. The singly occupied molecular orbital (SOMO) for each $[M(mnt)_2]^{1-}$ is of b_{2g} symmetry and equivalent to the HOMO of $[M(mnt)_2]^{2-}$ (Figure 6).[10,18,19] A molecular orbital energy level diagram for the eight highest occupied α-spin and the corresponding β-spin orbitals of $[Ni(mnt)_2]^{1-}$ (fixed at the geometry of $[Ni(mnt)_2]^{2-}$) is given in Figure 8. The calculations predict some change in the energies and ordering of these orbitals relative to $[Ni(mnt)_2]^{2-}$ (Figures 7, 8). In particular, the closer spacings among the

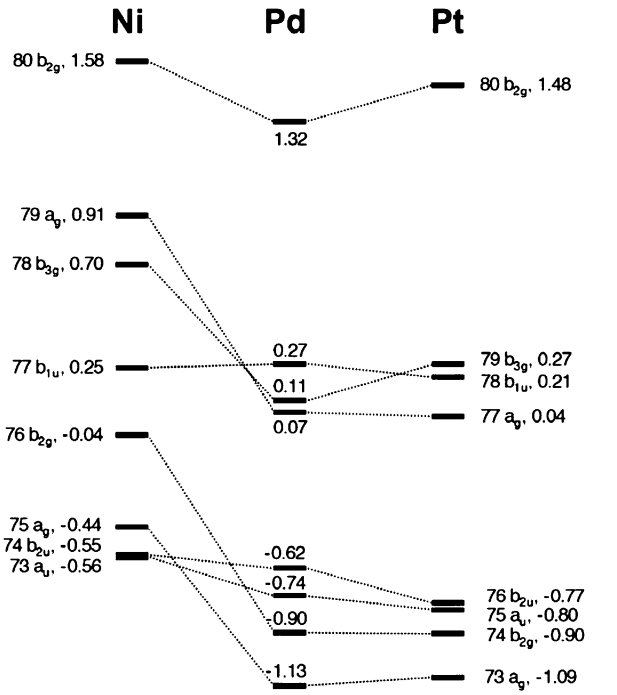

Figure 7. Correlation diagram relating the predicted energies for the eight highest occupied orbitals for $[M(mnt)_2]^{2-}$ (see also Figure 6).

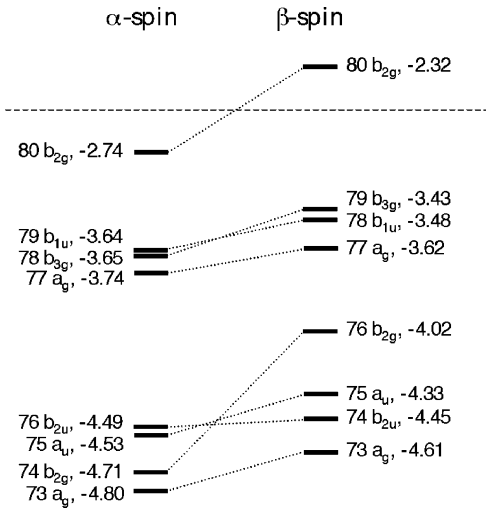

Figure 8. Calculated molecular orbital energy levels for $[Ni(mnt)_2]^{1-}$. The corresponding α- and β-spin orbitals are connected by dotted lines. The α-spin orbital $80b_{2g}$ is occupied, but the corresponding β-spin orbital is vacant.

highest energy occupied b_{1u}, b_{3g}, and a_g levels for $[Ni(mnt)_2]^{1-}$ relative to $[Ni(mnt)_2]^{2-}$ are consistent with orbital energy levels proposed recently for $[Ni(S_2C_2Me_2)_2]^{n-}$.[19,46] Energy level diagrams and MO pictures for each $[M(mnt)_2]^{1-}$ calculated at the geometry of the parent $[M(mnt)_2]^{2-}$ are provided in the Supporting Information (Figures S3—S5).

Electron detachment from the HOMO-1, HOMO-2, etc. of the parent $[M(mnt)_2]^{2-}$ accesses excited states of the product $[M(mnt)_2]^{1-}$, giving rise to bands A, B, etc., in the photoelectron spectra. Within the single particle approximation, these excited states are equivalent to those arising from one-electron transitions from the doubly occupied orbitals in the ground state of $[M(mnt)_2]^{1-}$ to the SOMO (β80 b_{2g}). The energies of the relevant excited states were predicted using TD-DFT calculations and are summarized in Table 3. Although not relevant to

Table 3. TD-DFT Calculated Excitation Energies (eV) and Oscillator Strengths (f_{calcd}) for One-Electron Excitations from Occupied β-spin MOs of $[M(mnt)_2]^{1-}$ to the SOMO (80 b_{2g}) That Is Doubly Occupied in $[M(mnt)_2]^{2-}$[a]

$[Ni(mnt)_2]^-$			$[Pd(mnt)_2]^-$			$[Pt(mnt)_2]^-$		
MO	energy	$f_{calcd} \times 10^3$	MO	energy	$f_{calcd} \times 10^3$	MO	energy	$f_{calcd} \times 10^3$
79 b_{3g}	1.00	0.0	79 b_{1u}	1.28	94	79 b_{1u}	1.46	107
78 b_{1u}	1.42	81	78 b_{3g}	1.35	0.0	78 b_{3g}	1.32	0.0
77 a_g	1.06	0.0	77 a_g	1.54	0.0	77 a_g	1.74	0.0
76 b_{2g}	1.86	0.0	76 b_{2u}	1.96	0.0	76 a_u	2.35	6.2
75 a_u	2.18	6.2	75 a_u	2.18	7.2	75 b_{2u}	2.25	0.0
74 b_{2u}	2.13	0.0	74 b_{2g}	2.45	0.0	74 b_{2g}	2.51	0.0
73 a_g	2.03	0.0	72 a_g	2.61	0.0	73 a_g	2.70	0.0

[a] Calculated with the geometry of $[M(mnt)_2]^-$ fixed at that of $[M(mnt)_2]^{2-}$.

Table 4. Theoretical Vertical Detachment Energies (VDE, eV) and Assignments for Detachment from the HOMO to HOMO-7 Levels of $[M(mnt)_2]^{2-}$ (see also Figures 6, 7)

$[Ni(mnt)_2]^{2-}$			$[Pd(mnt)_2]^{2-}$			$[Pt(mnt)_2]^{2-}$		
MO[a]	VDE	feature[b]	MO[a]	VDE	feature[b]	MO[a]	VDE	feature[b]
80 b_{2g}	0.37	X	80 b_{2g}	0.57	X	80 b_{2g}	0.43	X
79 a_g	1.43	B	79 b_{1u}	1.85	A	79 b_{3g}	1.75	A
78 b_{3g}	1.37	A	78 b_{3g}	1.92	B	78 b_{1u}	1.89	B
77 b_{1u}	1.79	C	77 a_g	2.11	C	77 a_g	2.17	C
76 b_{2g}	2.23	D	76 b_{2u}	2.53	D	76 b_{2u}	2.68	D
75 a_g	2.40	E	75 a_u	2.75	E	75 a_u	2.78	D
74 b_{2u}	2.50	E	74 b_{2g}	3.02	F	74 b_{2g}	2.94	E
73 a_u	2.55	E	73 a_g	3.18	G	73 a_g	3.13	E

[a] Refers to the MOs of $[M(mnt)_2]^{2-}$ (Figure 7). [b] Refers to the experimental detachment features (Table 1, Figures 2−4).

Table 5. Theoretical Vertical Detachment Energies (eV) for Detachment from $[M(mnt)_2]^{1-}$ ($^2B_{2g}$) to the Lowest Energy Singlet (^1A_g) and Triplet ($^3B_{3u}$) States of $[M(mnt)_2]$ (M = Ni, Pd, Pt)

detachment	$[Ni(mnt)_2]^{1-}$	$[Pd(mnt)_2]^{1-}$	$[Pt(mnt)_2]^{1-}$
$^2B_{2g} \rightarrow {}^1A_g$	4.57	4.58	4.48
$^2B_{2g} \rightarrow {}^3B_{3u}$	5.33	5.22	5.29

the present experiments, calculated oscillator strengths (f_{calcd}) are included to aid with comparison of solution phase electronic absorption data. Theoretical VDEs were derived from the difference in energy between the ground state of the parent $[M(mnt)_2]^{2-}$ and the ground and excited states of the product $[M(mnt)_2]^{1-}$ with its geometry fixed at that of $[M(mnt)_2]^{2-}$ (i.e., vertical detachment). These are detailed in Table 4 and illustrated as vertical bars on the 193 nm spectra of Figures 2−4.

The singly charged anions $[M(mnt)_2]^{1-}$ were also examined by PES (Figure 5). Geometries and MO energy levels and pictures for each $[M(mnt)_2]^{1-}$ at their optimized geometry are included in the Supporting Information (Table S2, Figures S6−S8). Electron detachment from the doublet ground states of these anions can give rise to singlet and triplet states of neutral $[M(mnt)_2]$. The ground states for each $[M(mnt)_2]$ were calculated as ^1A_g, consistent with experimental observations that related species are diamagnetic ($S = 0$).[10] The lowest energy triplet states for each $[M(mnt)_2]$ were calculated as $^3B_{3u}$, with unpaired electrons in orbitals equivalent to the HOMO (80 b_{2g}) and HOMO-3 (77 b_{1u}) of $[Ni(mnt)_2]^{2-}$ (Figures 1, 6). The calculated VDEs for the $^2B_{2g} \rightarrow {}^1A_g$ and $^2B_{2g} \rightarrow {}^3B_{3u}$ detachment transitions are detailed in Table 5 and marked on the spectra of Figure 5 as blue and green vertical bars, respectively. Additional TD-DFT calculations (data not shown) suggested the first singlet excited state for each $[M(mnt)_2]$ was at least a further 0.5 eV higher in energy than the $^3B_{3u}$ state.

Discussion

Spectral Assignment for the Dianions $[M(mnt)_2]^{2-}$ (M = Ni, Pd, Pt). Detachment features in the PES spectra of $[M(mnt)_2]^{2-}$ arise from transitions from the ground states of $[M(mnt)_2]^{2-}$ to the ground and excited states of $[M(mnt)_2]^{1-}$ (Table 3, 4). Theoretical predictions for the first VDEs for each $[M(mnt)_2]^{2-}$ were derived from the difference in energy between the ground states of the parent $[M(mnt)_2]^{2-}$ and the one-electron detached species with its geometry fixed at that of $[M(mnt)_2]^{2-}$. These were in good agreement with experiment (Table 4). In particular, trends in the predicted VDEs as a function of metal mirrored those observed experimentally (i.e., Ni ≈ Pt < Pd; Table 1) and that expected based on the relative energies of the HOMOs (Figure 7). The remaining features in the photoelectron spectra of Figures 2−4 correspond to excited states of the monoanions $[M(mnt)_2]^{1-}$ and were assigned on the basis of the TD-DFT calculations (Tables 3, 4). The relationship between the ground state of parent $[Ni(mnt)_2]^{2-}$ and the ground state and the first three excited states of product $[Ni(mnt)_2]^{1-}$ is schematically illustrated in Figure 9a.

A. PES features of $[Ni(mnt)_2]^{2-}$ and excited states of $[Ni(mnt)_2]^{1-}$. Features A and B in the PES spectra of $[Ni(mnt)_2]^{2-}$ correspond to the first and second excited states, respectively, of the monoanion $[Ni(mnt)_2]^{1-}$. The TD-DFT calculations predicted two low energy excited states for $[Ni(mnt)_2]^{1-}$ arising from the one-electron transitions β79 $b_{3g} \rightarrow \beta$80 b_{2g} and β77 $a_g \rightarrow \beta$80 b_{2g}, respectively (Table 3, Figure 8). These states are equivalent to those accessed directly by electron detachment from the HOMO-2 (78 b_{3g}) and HOMO-1 (79 a_g), respectively, of the parent $[Ni(mnt)_2]^{2-}$ (Figures 6, 9). The VDEs to access these states were calculated as 1.37 and 1.43 eV (Table 4), in good agreement with the measured VDEs for features A and B (1.35 and 1.48 eV, respectively; Table 1). The third excited state of $[Ni(mnt)_2]^{1-}$ is predicted to arise from the transition β78 $b_{1u} \rightarrow \beta$80 b_{2g} and is equivalent to that accessed directly by detachment from HOMO-3 (77 b_{1u}) of $[Ni(mnt)_2]^{2-}$ (Table 4, Figures 6, 9). This is predicted to occur at a VDE of 1.79 eV, in good agreement with the experimental VDE of feature C (1.90 eV, Table 1). The next four excited states of $[Ni(mnt)_2]^{1-}$ are predicted to be separated by only 0.3 eV and occur in the region of band E and the weaker shoulder labeled D. The high density of states predicted for this region is in qualitative agreement with the experimentally observed spectral density but prevents a more detailed assignment.

B. PES Features of $[Pd(mnt)_2]^{2-}$ and Excited States of $[Pd(mnt)_2]^{1-}$. The HOMO-1 of $[Pd(mnt)_2]^{2-}$ is a ligand-based orbital equivalent to the HOMO-3 of $[Ni(mnt)_2]^{2-}$ (b_{1u}, Figure 7). Detachment from this orbital is predicted to occur at a VDE of 1.85 eV (Table 4), in good agreement with the experimental VDE of feature A (1.87 eV, Table 1). Detachment from the equivalent orbital of $[Ni(mnt)_2]^{2-}$ occurred at a VDE of 1.90 eV, and the very similar electron binding energies for this orbital in both complexes are consistent with its ligand-based nature (Figure 6). In addition, these detachment features were both observed to undergo a significant increase in relative intensity at 266 nm (Figures 2, 3), providing further support for their common origin.

The HOMO-2 and HOMO-3 of $[Pd(mnt)_2]^{2-}$ are metal-based orbitals of b_{3g} and a_g symmetry, respectively (Figure 7). Detachment features from these orbitals were predicted to occur

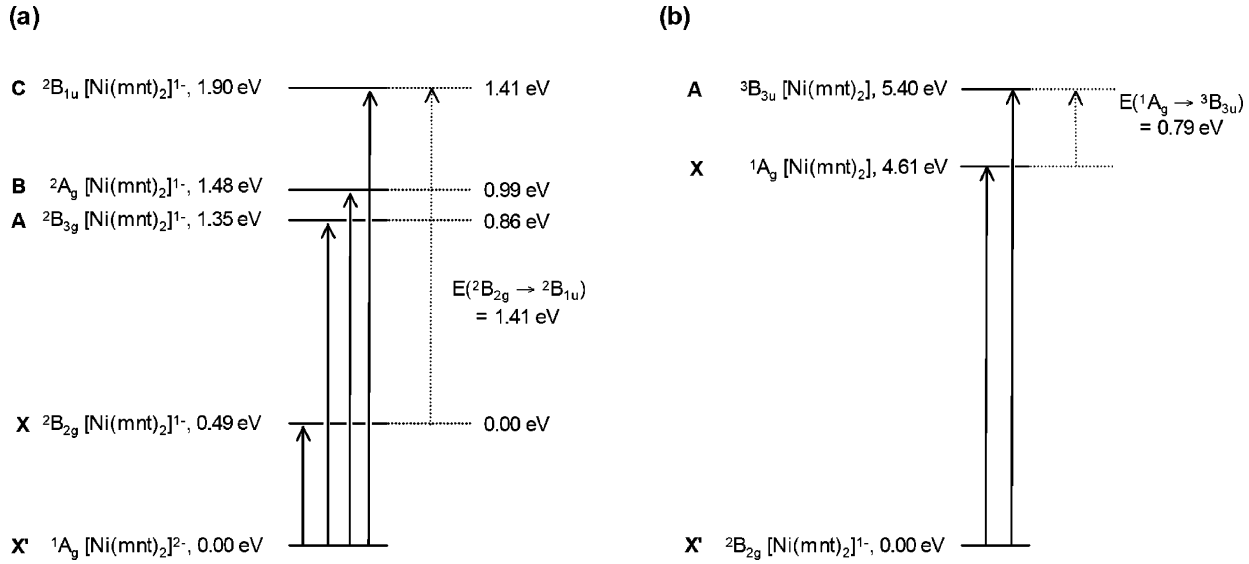

Figure 9. Schematic energy level diagrams indicating the relationship between the photodetachment transitions and excited states of $[Ni(mnt)_2]^{2-/1-/0}$. (a) The ground state of $[Ni(mnt)_2]^{2-}$ (X′) and the ground (X) and excited (A−C) states of $[Ni(mnt)_2]^{1-}$. The intense optical transition ($^2B_{2g} \rightarrow {}^2B_{1u}$) observed for $[Ni(mnt)_2]^{1-}$ in solution is shown. (b) The ground state of $[Ni(mnt)_2]^{1-}$ (X′) and the lowest energy singlet (X) and triplet (A) states of $[Ni(mnt)_2]$. The singlet−triplet splitting of $[Ni(mnt)_2]$ is shown.

at VDEs of 1.92 and 2.11 eV respectively (Table 4), in agreement with the measured VDEs of features B and C (Table 1). These metal-based detachment channels were shifted by ∼0.7 eV to higher binding energies from $[Ni(mnt)_2]^{2-}$ to $[Pd(mnt)_2]^{2-}$, consistent with the expected stabilization of the Pd 4d manifold relative to Ni 3d. Detachment from the ligand-based HOMO-4 and HOMO-5 orbitals of $[Pd(mnt)_2]^{2-}$ was predicted to occur at VDEs of 2.53 and 2.75 eV (Table 4), respectively, in good agreement with the measured VDEs of features D and E (Table 1). The HOMO-6 and HOMO-7 levels of $[Pd(mnt)_2]^{2-}$ are of b_{2g} and a_g symmetry, respectively (equivalent to the HOMO-4 and HOMO-5 of $[Ni(mnt)_2]^{2-}$, Figures 6, 7). Detachment features from these orbitals were predicted to occur at VDEs of 3.02 and 3.18 eV (Table 4), respectively, and close to measured VDEs of features F and G (Table 1). Detachment from these predominantly metal-based orbitals are again shifted to a higher binding energy from $[Ni(mnt)_2]^{2-}$ to $[Pd(mnt)_2]^{2-}$.

C. PES Features of $[Pt(mnt)_2]^{2-}$ and Excited States of $[Pt(mnt)_2]^{1-}$. The HOMO-1 of $[Pt(mnt)_2]^{2-}$ is predominantly metal-based and of b_{3g} symmetry (equivalent to the HOMO-2 of $[Ni(mnt)_2]^{2-}$, Figures 6, 7). Detachment from this orbital is predicted to occur at a VDE of 1.75 eV (Table 4), in agreement with the measured VDE of feature A (1.75 eV, Table 1). The HOMO-2 of $[Pt(mnt)_2]^{2-}$ is ligand based and of b_{1u} symmetry (equivalent to the HOMO-3 of $[Ni(mnt)_2]^{2-}$, Figures 6, 7). Detachment from this orbital is predicted to occur at a VDE of 1.89 eV (Table 4), in close agreement with the measured VDE of feature B (1.94 eV, Table 1). Detachment from the equivalent orbitals of $[Ni(mnt)_2]^{2-}$ and $[Pd(mnt)_2]^{2-}$ also occurred at very similar VDEs, consistent with the ligand-based nature of this orbital. In addition, features assigned to detachment from the b_{1u} orbital for each $[M(mnt)_2]^{2-}$ exhibited a significant increase in relative intensity at 266 nm, further supporting the spectral assignment.

Detachment from the HOMO-3 of $[Pt(mnt)_2]^{2-}$ was predicted to occur at a VDE of 2.17 eV (Table 4), in agreement with the VDE of feature C (2.05 eV, Table 1). Agreement between experiment and theory was poorer for the higher binding energy features (Figure 4). The theoretical VDEs for the HOMO-4 (b_{2u}) and HOMO-5 (a_u) are 2.68 and 2.78 eV, respectively, which are close in energy and might contribute to the strong feature labeled D in the 193 nm spectrum with a VDE of 2.50 eV (Figure 4c).

Comparison with Optical Absorption in Solution. Energy differences between PES spectral features for $[M(mnt)_2]^{2-}$ provide excitation energies for excited states of $[M(mnt)_2]^{1-}$ (Figure 9a). The vertical nature of the detachment process means that these data are obtained at the geometry of the parent $[M(mnt)_2]^{2-}$. The calculations indicated only very minor changes in MO levels between $[M(mnt)_2]^{1-}$ calculated at its relaxed geometry and at the geometry of the parent $[M(mnt)_2]^{2-}$ (Figures S3−S8), indicating that vertical excitation energies obtained in the present experiments are likely to be very close to those of $[M(mnt)_2]^{1-}$ at its relaxed geometry. This suggested comparison of excited-state energies from the present experiments with those from electronic absorption experiments in solution.

Features X and C for $[Ni(mnt)_2]^{2-}$ were assigned to detachment from the HOMO and HOMO-3 levels of $[Ni(mnt)_2]^{2-}$, respectively, giving rise to $^2B_{2g}$ and $^2B_{1u}$ states of $[Ni(mnt)_2]^{1-}$ (Figure 9). This suggested that the energetic separation between these features of 1.41 eV corresponds to the energy of the $^2B_{2g} \rightarrow {}^2B_{1u}$ transition for $[Ni(mnt)_2]^{1-}$ (Figures 9, 10). The TD-DFT calculations predicted the one-electron excitation β78 $b_{1u} \rightarrow \beta$80 b_{2g} to occur at 1.42 eV, in good agreement with the experimental separation (Table 3, Figures 9, 10). This transition occurs at similar energy to the intense optical absorption observed at about 1.45 eV in the electronic absorption spectrum of $[Ni(mnt)_2]^{1-}$ in solution, which is commonly assigned to an equivalent one-electron transition.[10,12,55,61] The high oscillator strength predicted for this transition is consistent with its intensity in the electronic absorption spectrum (Table 3). Similarly, the energy of the corresponding excited state for $[Pd(mnt)_2]^{1-}$ is estimated from the separation between features X and A as 1.14 eV (Figure 10), which is again in good

(61) Schrauzer, G. N.; Mayweg, V. P. *J. Am. Chem. Soc.* **1965**, *87*, 3585.

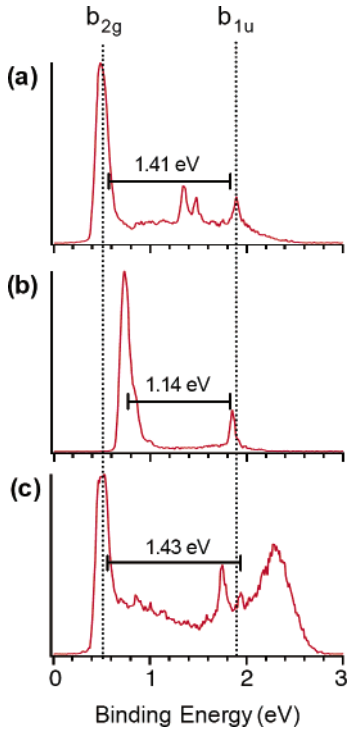

Figure 10. Comparison of the 355 nm photoelectron spectra of (a) $[Ni(mnt)_2]^{2-}$, (b) $[Pd(mnt)_2]^{2-}$, and (c) $[Pt(mnt)_2]^{2-}$. The dashed lines at 0.5 and 1.9 eV are to guide the eye and illustrate the change in binding energies of the b_{2g} and b_{1u} detachment features as a function of the metal center.

agreement with the energy of the intense $^2B_{2g} \rightarrow {}^2B_{1u}$ transition observed at 1.12 eV in solution.[12] The corresponding transition for $[Pt(mnt)_2]^{1-}$ is estimated from the separation between bands X and B as 1.43 eV (Figure 10), also in good agreement with the energy of the intense feature observed at 1.45 eV for $[Pt(mnt)_2]^{1-}$ in solution.[12]

The intense $^2B_{2g} \rightarrow {}^2B_{1u}$ transition observed for $[M(mnt)_2]^{1-}$ and related dithiolene centers commonly occurs at similar energies for $[Ni(S_2C_2R_2)_2]^{1-}$ and $[Pt(S_2C_2R_2)_2]^{1-}$ but at lower energies for $[Pd(S_2C_2R_2)_2]^{1-}$.[10,12,22,29] The donor orbital is purely ligand based (b_{1u}, doubly occupied) and occurs at similar orbital energies for each species because it is of incorrect symmetry to interact with the metal d-orbitals. Consequently, detachment from this orbital occurrs at 1.9 eV for each $[M(mnt)_2]^{2-}$ independent of the metal center (Figures 7, 10). In contrast, the acceptor orbital (b_{2g}, singly occupied) contains some metal character and is stabilized from Ni to Pd but destabilized from Pd to Pt (Figures 7, 10). Consequently, detachment from this orbital occurs at similar binding energies for $[Ni(mnt)_2]^{2-}$ and $[Pt(mnt)_2]^{2-}$ but 0.25 eV higher binding energy for $[Pd(mnt)_2]^{2-}$. These shifts result in a smaller spacing between detachment features arising from the b_{2g} and b_{1u} orbitals for $[Pd(mnt)_2]^{2-}$ and reduced separation between the $^2B_{2g}$ ground and $^2B_{1u}$ excited states of $[Pd(mnt)_2]^{1-}$ (Figure 10).

Comparison between $[Ni(mnt)_2]^{2-}$ and $[MoO(mnt)_2]^{2-}$. The electronic structure of the square-pyramidal anion $[MoO(mnt)_2]^{2-}$ has been studied previously by PES and DFT calculations,[34] allowing for direct comparison with $[Ni(mnt)_2]^{2-}$. Detailed MO pictures for $[MoO(mnt)_2]^{2-}$ can be found in a previous publication.[34] Qualitatively similar ligand-based orbitals can be identified for both species, despite the different metal center, oxidation state, and coordination geometry. The HOMO of $[MoO(mnt)_2]^{2-}$ is the nonbonding metal-based orbital Mo $4d_{x^2-y^2}$ that is doubly occupied in this formally d^2 center, and is equivalent to the HOMO-5 of $[Ni(mnt)_2]^{2-}$ (Figure 6). The HOMO-1 and HOMO-2 of $[MoO(mnt)_2]^{2-}$ are dithiolene ligand-based orbitals that are qualitatively very similar to the HOMO and HOMO-3 of $[Ni(mnt)_2]^{2-}$ (Figure 6). These orbitals arise from the asymmetric and symmetric combinations, respectively, of the highest energy occupied dithiolene π-type orbital on each ligand (Figure 6, 80 b_{2g} and 77 b_{1u}, respectively). The origin and energetic splitting of these orbitals has been described in detail previously for the related species $[Ni(S_2C_2Me_2)]^{2-}$.[19] The splitting between these levels arises from a combination of ligand-ligand interaction (b_{2g}, antibonding and b_{1u}, bonding) and destabilization of the b_{2g} level due to the presence of Ni $3d_{xz}$ antibonding character (Figure 6).[19] The splitting between these levels for $[Ni(mnt)_2]^{2-}$ was measured in the present study as 1.4 eV, while that for the equivalent orbitals of $[MoO(mnt)_2]^{2-}$ was measured previously as 0.7 eV.[34] The reduced splitting for $[MoO(mnt)_2]^{2-}$ is consistent with destabilization of the Mo $4d_{xz,yz}$ levels due to the strong field oxo ligand,[10] which results in significantly less Mo $4d_{xz}$ character in the asymmetric combination and less destabilization of this orbital.[34] Indeed, the separation between these orbitals of 0.7 eV for $[MoO(mnt)_2]^{2-}$ is close to a previous estimate of 0.5 eV for splitting due to ligand-ligand interaction alone,[19,62] and further reinforces the significant destabilization of the HOMO of $[Ni(mnt)_2]^{2-}$ due to the presence of Ni $3d_{xz}$ antibonding character (Figure 6).

Spectral Assignments for the Monoanions $[M(mnt)_2]^{1-}$ (M = Ni, Pd, Pt). The spectra for $[M(mnt)_2]^{1-}$ each exhibit a lower binding energy feature (X, ~4.5 eV) and a series of overlapping features at higher binding energies (A−C). These overlapping features are consistent with the open shell nature of the parent $[M(mnt)_2]^{1-}$ ($^2B_{2g}$) and the possibility for detachment to singlet and triplet states of the neutral product $[M(mnt)_2]$. The spectral density makes a detailed assignment of the higher binding energy features difficult. The singlet ground state ^1A_g of neutral $[M(mnt)_2]$ is accessed by electron detachment from the singly occupied b_{2g} orbital of $[M(mnt)_2]^{1-}$ (e.g. $[Ni(mnt)_2]^{1-}$, Figures 8, 9b), and the calculated VDEs for this transition agree well with the experimental VDEs of feature X for each of $[M(mnt)_2]^{1-}$ (Tables 2, 5). The calculations also predicted the lowest energy triplet state for each of $[M(mnt)_2]$ to be $^3B_{3u}$, which is accessed by detachment of a β-spin electron from the doubly occupied b_{1u} orbital of the parent $[M(mnt)_2]^{1-}$ (Figures 8, 9b). The calculated VDEs for this detachment transition agree well with the measured VDEs of feature A for each of $[M(mnt)_2]^{1-}$ (Tables 2, 5). Additional TD-DFT calculations on neutral $[M(mnt)_2]$ (data not shown) indicated that the first singlet excited states for each of $[M(mnt)_2]$ were at least a further 0.5 eV higher in energy than their $^3B_{3u}$ states, and suggested that feature A should be due to the $^3B_{3u}$ state and not the first singlet excited state. This suggested that the separation between features X and A in the PES spectra define the singlet−triplet splitting in the neutral $[M(mnt)_2]$ complexes (Figure 9b). As described above, the vertical nature of the detachment process means that these

(62) The splitting of the b_{2g} and b_{1u} levels of $[Ni(S_2C_2Me_2)]^{2-}$ due to ligand−ligand interaction (antibonding and bonding respectively) has been estimated as 0.5 eV on the basis of calculations on the free dithiolene ligands $[(S_2C_2Me_2)_2]^{4-}$ fixed at the geometry of $[Ni(S_2C_2Me_2)]^{2-}$ but without the Ni^{2+} center (see ref 19). Equivalent calculations for $[(mnt)_2]^{4-}$ at the geometry of $[Ni(mnt)_2]^{2-}$ suggest an identical estimate of 0.5 eV is also appropriate in the present case.

estimates correspond to the vertical singlet−triplet splitting of neutral $[M(mnt)_2]$ with their geometry fixed at that of parent $[M(mnt)_2]^{1-}$. However, the very similar geometries of $[M(mnt)_2]^{1-}$ and $[M(mnt)_2]$ suggest that these estimates are likely to be very close to that of $[M(mnt)_2]$ at its relaxed geometry.

The singlet−triplet splitting for a range of neutral bis(dithiolene) centers has been estimated in recent theoretical studies, and proposed as an indication of the extent of singlet-diradical character in the ground-state wave function of neutral $[M(S_2C_2R_2)_2]$.[27−29] Studies based on DFT predicted splittings of ∼0.6 eV for both of $[Ni(S_2C_2Me_2)_2]$ and $[Ni(S_2C_6H_4)_2]$, and about 0.45 eV for $[Ni(S_2C_2H_2)_2]$,[19,27,28] while a recent study based on multiconfigurational ab inito calculations predicted a larger value of 1.2 eV for $[Ni(S_2C_6H_4)_2]$.[29] Experimental data does not appear to be available. The present PES data yield directly the singlet−triplet splitting in $[M(mnt)_2]$ as 0.79, 0.57 and 0.83 eV for M = Ni, Pd, and Pt, respectively. The reduced singlet−triplet splitting for $[Pd(mnt)_2]$ is consistent with the reduced separation between the b_{1u} and b_{2g} orbitals for the dianion $[Pd(mnt)_2]^{2-}$ (Figures 7, 9), and similar trends as a function of metal predicted for the related species $[M(S_2C_6H_4)_2]$ (M = Ni, Pt, Pd).[29]

Relationship Between Detachment Energies and Oxidation Potentials. Electron detachment in the gas phase is similar to a one-electron oxidation in solution.[63] The ADEs for $[M(mnt)_2]^{2-}$ can be compared with the oxidation energies of the same species in solution. The ADEs of $[Ni(mnt)_2]^{2-}$ and $[Pt(mnt)_2]^{2-}$ are almost identical, while that for $[Pd(mnt)_2]^{2-}$ is about 0.25 eV higher (Table 1). An equivalent trend is observed in solution, where $[Ni(mnt)_2]^{2-}$ and $[Pt(mnt)_2]^{2-}$ are oxidized at similar potentials, while that for $[Pd(mnt)_2]^{2-}$ is about ∼0.2−0.35 V more positive.[12,55]

Trends observed for the singly charged species $[M(mnt)_2]^{1-}$ also parallel those observed in solution. The ADEs for $[Ni(mnt)_2]^{1-}$ and $[Pd(mnt)_2]^{1-}$ were similar, while that for $[Pt(mnt)_2]^{1-}$ was about 0.1 eV lower (Table 2). This correlates with solution phase data, where $[Pt(mnt)_2]^{1-}$ is about 0.1 V more easily oxidized than $[Ni(mnt)_2]^{1-}$ and $[Pd(mnt)_2]^{1-}$.[64] The close correspondence between gas-phase detachment energies and solution phase oxidation potentials suggest that differences are due to the intrinsic electronic structure of each of $[M(mnt)_2]^{2-}$ and $[M(mnt)_2]^{1-}$, and that the effects of solvation are similar for each species.

Conclusions

The bis(dithiolene) anions $[M(mnt)_2]^{2-}$ and $[M(mnt)_2]^{1-}$ (M = Ni, Pd, Pt) were transferred to the gas phase by electrospray and their intrinsic electronic structure studied by photodetachment photoelectron spectroscopy. The experimental data were interpreted with the aid of DFT calculations on the ground states of $[M(mnt)_2]^{2-}$ and the ground and excited states of $[M(mnt)_2]^{1-}$ and $[M(mnt)_2]$.

Spectral features for detachment from the closed shell dianions $[M(mnt)_2]^{2-}$ provided a direct picture of the MO energy levels of these species. The PES spectra for $[Ni(mnt)_2]^{2-}$ were consistent with the calculated MO energy levels (Figure 6) as well as those proposed previously for the related species $[Ni(S_2C_2Me_2)]^{2-}$.[19,46] The experiments demonstrate the similar energies of the highest energy occupied dithiolene- and metal-based orbitals, and reinforce the noninnocent nature of the dithiolene ligand[15] and the inverted level bonding scheme proposed for these centers.[10,19]

Detachment features arising from ligand-based orbitals were observed to occur at similar electron binding energies for each of $[M(mnt)_2]^{2-}$ (M = Ni, Pd, Pt), independent of the metal center, while those from metal-based orbitals were shifted to higher binding energies for the heavier congeners (M = Pd, Pt). The first feature for each of $[M(mnt)_2]^{2-}$ was assigned to detachment from the HOMO that is ligand-based with some metal d_{xz} contribution. The energetic shifts of this feature for $[M(mnt)_2]^{2-}$ were consistent with the covalent nature of this orbital and its sensitivity to changes in both metal center and M−S bond lengths.

The separation between PES spectral features of $[M(mnt)_2]^{2-}$ provided information about the relative energies of excited states of the product $[M(mnt)_2]^{1-}$. In particular, the separation between features assigned to detachment from the frontier b_{2g} and b_{1u} orbitals of $[M(mnt)_2]^{2-}$ provide estimates for the energy of the $^2B_{2g} \rightarrow {}^2B_{1u}$ transition that is observed as an intense feature in the electronic absorption spectrum of $[M(mnt)_2]^{1-}$. The present data demonstrate that the donor orbital in this transition (b_{1u}) occurs at similar energies for each species, and that the reduced energy of this absorption for $[Pd(mnt)_2]^{1-}$ is due to stabilization of the acceptor orbital (b_{2g}).

PES of the singly charged anions $[M(mnt)_2]^{1-}$ provided access to the lowest energy singlet and triplet states of neutral $[M(mnt)_2]$, allowing an experimental measurement of the singlet−triplet splittings in these species. The reduced singlet−triplet splitting for $[Pd(mnt)_2]$ is consistent with the observed stabilization of the HOMO of $[Pd(mnt)_2]^{2-}$ (equivalent to the LUMO of neutral $[Pd(mnt)_2]$).

Acknowledgment. This work was supported by the National Science Foundation (CHE-0349426) and the John Simon Guggenheim Foundation and performed at the W. R. Wiley Environmental Molecular Sciences Laboratory (EMSL), a national scientific user facility sponsored by DOE's Office of Biological and Environmental Research and located at Pacific Northwest National Laboratory, which is operated for the DOE by Battelle. All calculations were performed using the EMSL Molecular Science Computing Facility (MSCF).

Supporting Information Available: Full list of authors for refs 49 and 50. Cartesian coordinates and energies for the optimized geometries of $[M(mnt)_2]^{2-}$ and $[M(mnt)_2]^{1-}$ (Tables S1, S2), molecular orbital contour plots for the eight highest occupied orbitals of $[Pd(mnt)_2]^{2-}$ and $[Pt(mnt)_2]^{2-}$ (Figure S1, S2), $[M(mnt)_2]^{1-}$ at the geometry of $[M(mnt)_2]^{2-}$ (Figures S3-S5) and $[M(mnt)_2]^{1-}$ at its relaxed geometry (Figures S6-S8). This material is available free of charge via the Internet at http://pubs.acs.org. See any current masthead page for ordering information and Web access instructions.

JA056342S

(63) Wang, X. B.; Wang, L. S. *J. Chem. Phys.* **2000**, *112*, 6969.
(64) Geiger, W. E.; Barriere, F.; LeSuer, R. J.; Trupia, S. *Inorg. Chem.* **2001**, *40*, 2472.